Proteomic analysis of the pyrenoid-traversing membranes of *Chlamydomonas reinhardtii* reveals novel components

Eric Franklin[1], Lianyong Wang[1], Edward Renne Cruz[1], Keenan Duggal[1], Sabrina L. Ergun[1,2], Aastha Garde[1,2], Martin C. Jonikas[1,2]

[1]Department of Molecular Biology, Princeton University, Princeton, NJ 08544, USA
[2]Howard Hughes Medical Institute, Princeton University, Princeton, NJ 08544, USA

Summary

- Pyrenoids are algal CO_2-fixing organelles that mediate approximately one-third of global carbon fixation and hold the potential to enhance crop growth if engineered into land plants. Most pyrenoids are traversed by membranes that are thought to supply them with concentrated CO_2. Despite the critical nature of these membranes for pyrenoid function, they are poorly understood, with few protein components known in any species.
- Here we identify protein components of the pyrenoid-traversing membranes from the leading model alga *Chlamydomonas reinhardtii* by affinity purification and mass spectrometry of membrane fragments. Our proteome includes previously-known proteins as well as novel candidates.
- We further characterize two of the novel pyrenoid-traversing membrane-resident proteins, Cre10.g452250, which we name Pyrenoid Membrane Enriched 1 (PME1), and LCI16. We confirm their localization, observe that they physically interact, and find that neither protein is required for normal membrane morphology.
- Taken together, our study identifies the proteome of pyrenoid-traversing membranes and initiates the characterization of a novel pyrenoid-traversing membrane complex, building toward a mechanistic understanding of the pyrenoid.

Key words: Affinity purification, *Chlamydomonas reinhardtii*, CO_2-concentrating mechanism (CCM), mass spectrometry, membranes, membrane proteins, proteomics, pyrenoid

Introduction

Globally, photosynthetic organisms fix over 100 billion metric tons of carbon each year via the conserved enzyme Ribulose-1,5-bisphosphate carboxylase/oxygenase (Rubisco), thought to be the most abundant protein in the world (Ellis, 1979; Field *et al.*, 1998; Beardall & Raven, 2020). Despite its importance to the biosphere, Rubisco runs relatively slowly for an enzyme in central carbon metabolism and is prone to catalyzing oxygenation, a wasteful reaction with abundant oxygen (Flamholz *et al.*, 2019). Some organisms overcome these limitations through the use of CO_2-concentrating mechanisms (CCMs). These mechanisms improve the efficiency of carbon fixation by concentrating CO_2 locally around Rubisco to increase its rate of carboxylation and decrease unwanted oxygenation (Hatch, 1987; Lüttge, 2004; Sage *et al.*, 2012; Raven *et al.*, 2017).

Eukaryotic algae, which mediate most of the CO_2 assimilation in the oceans (Mackinder, 2017), nearly all use a CCM based on a chloroplast-localized organelle called the pyrenoid (Wang *et al.*, 2015; Beardall & Raven, 2020; Meyer *et al.*, 2020a; Barrett *et al.*, 2021; He *et al.*, 2023). A pyrenoid is formed by tightly clustering the cell's Rubisco into a biomolecular condensate (Freeman Rosenzweig *et al.*, 2017). Concentrated CO_2 is released inside this condensate, increasing the carboxylation rate of Rubisco and decreasing its oxygenation. Despite their importance to the global carbon cycle, pyrenoids remain understudied and poorly understood at a molecular level.

Because pyrenoids evolved many times across independent algal lineages (Meyer *et al.*, 2020a; Barrett *et al.*, 2021; He *et al.*, 2023), many of the specific genes involved in CCM function differ between phylogenetic groups. However, we expect that common principles of biogenesis and function underlie these convergently-evolved structures. Our approach to uncovering these principles is to study the leading model alga, *Chlamydomonas reinhardtii* (*C. reinhardtii* hereafter), whose pyrenoid is currently best understood. The existence of an extensive experimental toolbox in this organism—including well-defined genetic and proteomic protocols and a library of knockout mutants—makes it a powerful platform for the discovery and characterization of novel pyrenoid components.

The *C. reinhardtii* pyrenoid consists of a phase-separated matrix containing tightly-packed Rubisco (Freeman Rosenzweig *et al.*, 2017), surrounded by a starch sheath that appears to limit CO_2 leakage (Toyokawa *et al.*, 2020; Fei *et al.*, 2022). Traversing the matrix are specialized

membranes that are thought to mediate the delivery of concentrated CO_2 to the matrix (Raven, 1997; Karlsson *et al.*, 1998; Sinetova *et al.*, 2012; Fei *et al.*, 2022).

In *C. reinhardtii* the pyrenoid-traversing membranes form a network of tubules that is contiguous with but ultrastructurally distinct from the photosynthetic thylakoid membranes (Engel *et al.*, 2015). Tubules are constitutively present including during cell division (Goodenough, 1970), in non-CCM-requiring growth conditions (Ma *et al.*, 2011; Caspari *et al.*, 2017), and in mutants deficient in pyrenoid matrix formation (Goodenough & Levine, 1970; Ma *et al.*, 2011; Mackinder *et al.*, 2016; Caspari *et al.*, 2017; He *et al.*, 2020). The tubules are structurally complex, being composed of a central reticulated region with three-way junctions out of which radiate discrete cylindrical tubules, which themselves contain smaller minitubules that are apparently also made of membranes (Engel *et al.*, 2015). The tubules are organizationally dynamic, with tubule quantity and diameter varying under different growth conditions (Rawat *et al.*, 1996). Given the presence of the tubules in the absence of a pyrenoid matrix, it has been proposed that they play an organizational role in pyrenoid nucleation or localization (Meyer *et al.*, 2020b), while their presence in non-CCM-requiring growth conditions suggests possible additional functions beyond CO_2 delivery.

To date, several tubule-localized proteins have been identified with varying degrees of confidence. The best-established proteins that localize specifically to the tubules are Carbonic AnHydrase 3 (CAH3; Cre09.g415700), which is thought to deliver CO2 to the pyrenoid; MIssing THylakoids 1 (MITH1; Cre06.g259100), which is necessary for producing pyrenoid-traversing membranes (Hennacy *et al.*, 2024); and Rubisco-Binding Membrane Protein 1/Bestrophin 4 (RBMP1/BST4, Cre06.g261750) and RBMP2 (Cre09.g416850), whose functions remain poorly characterized (Meyer *et al.*, 2020b).

Multiple strategies have been employed to isolate and identify *C. reinhardtii* pyrenoid proteins, including fractionation of whole pyrenoids (Mackinder *et al.*, 2016; Zhan *et al.*, 2018), systematic protein localization and affinity purification of protein complexes using known pyrenoid components as baits (Mackinder, 2017; Wang *et al.*, 2023), and proximity labeling of pyrenoid proteins using TurboID (Lau *et al.*, 2023).

Here, we identify tubule-localized proteins by developing a complementary approach that relies on isolating fragments of pyrenoid-traversing membranes. We show that the approach

successfully recovers known tubule proteins and identifies novel candidates. We further validate and characterize two of the top candidates. By expanding the known pyrenoid tubule proteome, this work contributes to paving the way toward a mechanistic understanding of pyrenoid function.

Materials and Methods

Strains and Culture Conditions

All insertional mutants were obtained from the CLiP collection at the Chlamydomonas Resource Center (Li *et al.*, 2019). Mutant IDs for these strains can be found in Table 1 below. The parent strain for these mutants is cMJ030 (CC-4533) and is also available from the Chlamydomonas Resource Center.

Unless otherwise noted, cultures were grown in TP media to a concentration of ~2×10^6 cells/mL prior to experiments. Unless otherwise noted, cultures were grown in low CO_2 (air, ~0.04% v/v CO_2) and 150 μmol · m^{-2} · s^{-1} photons.

All strains generated in this work were deposited to the Chlamydomonas Resource Center (https://chlamycollection.org).

Table 1. **Strains used in this work.**

Chlamydomonas Resource Center ID	Strain Description	Mating Type *(mt)*	Source	Antibiotic Resistance
CC-4533	Wild type CMJ030	*mt(-)*	Wild type and parent strain to CLiP library (Zhang *et al.*, 2014)	none
CC-5415	Wild type	*mt(+)*	Wild type and parent strain to *lci16-2*, *lci16-3*, and *lci16-4*	none
CC-5646	CMJ030;RBMP1-Venus-3×FLAG	*mt(-)*	Previously published (Meyer *et al.*, 2020b)	Paromomycin
CC-5647	CMJ030;RBMP2-	*mt(-)*	Previously published	Paromomycin

	Venus-3×FLAG		(Meyer *et al.*, 2020b)	
CSI_LW07G9	CMJ030;CPLD9-Venus-3×FLAG	*mt(-)*	CSI collection (Wang *et al.*, 2023)	Paromomycin
CSI_LW01C3	CMJ030;CGL129-Venus-3×FLAG	*mt(-)*	CSI collection (Wang *et al.*, 2023)	Paromomycin
	CMJ030;LCI16-Venus-3×FLAG	*mt(-)*	CMJ030 transformed with pLM005-LCI16-Venus-3×FLAG	Paromomycin
LMJ.RY0402.141937	*pme1-1*	*mt(-)*	CLiP library (Li *et al.*, 2019)	Paromomycin
LMJ.RY0402.168140	*pme1-2*	*mt(-)*	CLiP library (Li *et al.*, 2019)	Paromomycin
LMJ.RY0402.236076	*pme1-3*	*mt(-)*	CLiP library (Li *et al.*, 2019)	Paromomycin
LMJ.RY0402.215307	*lci16*	*mt(-)*	CLiP library (Li *et al.*, 2019)	Paromomycin

Table 2. **Primers used for PCR verification of insertional mutants**

Primer name	Sequence
TS.Hb.For	CGGTGATACTTACACGCCC
TS.Hb.Rev	CACAGTTTGTGTGGAATCGG
TIP.Q.For	CAGGGGAGTAGCAAAACAG
TIP.Q.Rev	GCTGCTTCATGTGACCTTG
TIP.Z4.For	CATAGAGCTTGCCATGTTATATCC
TIP.Z4.Rev	AGAAGGAGACGAAAGCACAGG
TIP.Z2/3.For	GGCTTGGATGACTGATGACCG
TIP.Z2/3.Rev	ACCTCGCCAATGCACAGACG

Membrane Affinity Purification and Mass Spectrometry

Detergent-based affinity purification of and mass spectrometry of RBMP1-Venus-3×FLAG, RBMP2-Venus-3×FLAG, and LCI16-Venus-3×FLAG were performed as described previously (Wang *et al.*, 2023).

For the membrane affinity purification, our objective was to isolate fragments of membranes of interest. We sought to achieve this by choosing baits localized to our membranes of interest and performing a standard affinity purification, as described in (Wang *et al.*, 2023), but with the membrane disruption step changed from dissolution with detergent to shearing with sonication. We used two bait proteins which localize to the tubules, RBMP1 (Cre06.g261750) and RBMP2 (Cre09.g416850) (Meyer *et al.*, 2020b), and two bait proteins for the thylakoids, CPLD9 (Cre01.g005001) and CGL129 (Cre05.g233950) (Wang *et al.*, 2023). We performed three iterations of this membrane affinity purification experiment, each with slight differences meant to better enrich membranes or detect the proteins enriched in the purification.

For the first membrane affinity purification, all steps—including cell growth, affinity purification, and mass spectrometry—were performed as in (Wang *et al.*, 2023), with the following changes: 1) any buffer with more than 0.1% digitonin was prepared without digitonin; 2) In place of membrane solubilization using IP buffer + digitonin followed by centrifugation at 12,700 × g, samples were instead sonicated with a probe sonicator (QSonica) in 20 cycles (5 x 1 sec. pulse, 30 sec. rest) in a microcentrifuge tube on ice followed by centrifugation at 1000 × g before progressing to incubation with anti-FLAG beads; 3) After elution and denaturation, samples were loaded into a 4-20% Criterion TGX Precast Mini Protean Gel (BioRad) for electrophoresis at 50 V for 40 min until the protein front moved ~2.0 cm to separate the FLAG peptides from the eluted proteins.

The second affinity purification replicated the first with the following additional changes: 1) Sonicated lysate was centrifuged at 5,000 × g; 2) In place of elution with FLAG peptide and in-gel digestion of proteins, proteins were digested on-bead using S-Trap™ Micro Spin Column Digestion (Protifi); 3) Samples were run on the mass spectrometer for 2 hours instead of 1 hour.

The third affinity purification was performed like the first with the following changes: 1) sonicated lysate was centrifuged at 5,000 × g; 2) after elution, samples were frozen and submitted to the Thermo Fisher Scientific Center for Multiplexed Proteomics at Harvard Medical School for

digestion, tandem mass tag (TMT) labeling (Thermo Fisher), and quantitative mass spectrometry (Ting *et al.*, 2011; McAlister *et al.*, 2012; Li *et al.*, 2020).

The full results for all three affinity purification experiments can be found in Supporting Information Tables **S1-3**.

Live-Cell Imaging

For live-cell imaging, strains expressing Venus-tagged proteins were grown at 3% CO_2 in TP media to a concentration of ~ 5×10^5 cells mL^{-1}, then transferred to ambient CO_2 16 hours before collecting for imaging at a concentration of ~1-2 × 10^6 cells mL^{-1}. 200 µL of each cell culture were placed into the wells of an 8-well µ-slide (Ibidi) and allowed to settle for 5 minutes. The culture media was aspirated to leave a thin layer of cells, and the cells were immobilized for imaging by flowing over 1 mL of 2% low-melting-point TP agarose in each well at ~40°C, which was allowed to set for 5 minutes at room temperature prior to imaging.

Cells were imaged using a VT-iSIM super-resolution spinning-disk confocal microscope on an Olympus iX83 body equipped with VisiView software, a 60X 1.43 NA objective and a Hamamatsu Orca Quest sCMOS camera in slow mode. Venus fluorescence was excited using a 514 nm laser and collected at 545/50 nm. Chlorophyll autofluorescence was excited using a 642 nm laser and collected at 700/75 nm. Confocal z-series were acquired with a 300 nm Z-step. The same acquisition settings were used for all strains imaged in this study. Images were imported into Fiji (Schindelin *et al.*, 2012) for deconvolution using the Microvolution plugin and final image preparation.

Transmission Electron Microscopy (TEM)

TEM was performed as described in (He *et al.*, 2020) with some modifications. Strains for TEM imaging were grown at 3% CO_2 in TP media to a concentration of ~5×10^5 cells mL^{-1}, then transferred to ambient CO_2 16 hours before harvesting at a concentration of ~1-2 × 10^6 cells mL^{-1}. At least 50×10^6 cells were harvested by centrifugation at 1,000 × g for 5 minutes in 50 mL tubes, resuspended in 1 mL TP, transferred to 1.5 mL screw-top tubes, and centrifuged again for 5 minutes at 1,000 x g. Cells were then resuspended in 2.5% gluteraldehyde in TP media (10 mL 10% gluteraldehyde, 30 mL TP) and nutated at room temperature for 1 hour. After nutation, cells were pelleted at 3,000 × g for 1 minute, then washed 3 times by resuspending and nutating in 1 mL ddH_2O for 5 minutes each, pelleting at 3,000 × g after each wash. Samples

were then post-fixed and stained with 1 mL freshly-prepared osmium tetroxide solution (1% OsO_4, 1.5% w/v $K_3[Fe(CN)_6]$, 2 mM $CaCl_2$) and nutated for 1-2 hours. Tubes were wrapped in aluminum foil during nutation to protect samples from light. Counterstaining with uranyl acetate was found to increase background staining and reduce contrast when looking at membranes, so for all images shown and analyzed here were stained using only OsO_4. Samples were then serially dehydrated by resuspension and nutation in increasing concentrations of ethanol: 5 minutes in 1 mL each of 30%, 50%, 70%, and 95% ethanol, then 10 minutes in 100% ethanol and 2 × 10 minutes in 100% acetonitrile. Samples were pelleted for 1 minute at 3,000 × g between each resuspension.

After dehydration, samples were embedded in epoxy resin containing 34% Quetol 651, 44% nonenyl succinic anhydride, 20% methyl-5-norbornene-2,3-dicarboxylic anhydride and 2% catalyst dimethylbenzylamine (Electron Microscopy Sciences) over four days, first by embedding overnight in 1:1 acetonitrile:resin (no catalyst) with the screw-top tube open in a fume hood, then by nutating in 1 mL Quetol resin (including catalyst) for four days, spinning down the samples and resuspending in fresh resin once per day. On day 4, the samples were resuspended in 300-500 µL resin, centrifuged at max speed (18,213 x g) for 20 minutes at 30°C in a tabletop centrifuge with a swinging bucket rotor for microfuge tubes, then cured at 60–65°C for 48 hours.

Thin (~70 nm) sections were prepared from cured resin blocks on a Leica Microtome Ultracut UCT and mounted on carbon film–coated 200 mesh copper TEM grids (Electron Microscopy Sciences) and imaged at the Imaging and Analysis Center, Princeton University, using a CM200 TEM (Philips) or a Talos F200X STEM (ThermoFisher Scientific).

Results

We used affinity purification to isolate membrane fragments

The use of affinity purification to identify protein complexes is well-documented (Morris *et al.*, 2014; Meyer & Selbach, 2015). Such methods usually involve the use of detergents during cell lysis to dissolve membranes (Behnke & Urner, 2023), such that proteins normally only co-precipitate with the bait protein if they are part of the same protein complex. This strategy has been used to identify novel protein complexes and elucidate functions for previously uncharacterized genes in Chlamydomonas (Mackinder, 2017; Wang *et al.*, 2023). However,

here we wanted to isolate fragments of tubule membrane, with the hopes that we could then comprehensively identify pyrenoid tubule-localized proteins.

We therefore adapted an existing affinity purification protocol used in *C. reinhardtii* (Mackinder, 2017; Wang *et al.*, 2023) to affinity purify intact membrane fragments. Using tagged membrane proteins of known localization (Fig. **1a**) as bait, we performed the affinity purification protocol on cell lysate in which membranes were disrupted by sonication rather than solubilized by detergent (Fig. **1b**). We reasoned that this approach would produce membrane fragments that would allow the identification of proteins that co-localized to the same regions of membranes even if they did not directly interact physically (Fig. **1c**).

We selected four bait proteins on which to perform this protocol: RBMP1-Venus-3×FLAG and RBMP2-Venus-3×FLAG (Fig. **1d,e**), which localize to the pyrenoid tubules (Meyer *et al.*, 2020b); and CPLD9-Venus-3×FLAG and CGL129-Venus-3×FLAG (Fig. **1f,g**), which localize to the thylakoid membranes and are excluded from the tubules (Wang *et al.*, 2023). RBMP1 and RBMP2 localize to distinct regions of the tubules—RBMP1 to the tubule periphery and RBMP2 to the central reticulated region (Meyer *et al.*, 2020b)—thus, we reasoned that together they should provide coverage for the whole tubule network. As expected from their distinct localizations, RBMP1 and RBMP2 did not co-precipitate via traditional detergent-based affinity purification (Fig. **1h**, Supporting Information Table **S4**).

Identification of a pyrenoid-traversing membrane proteome

We performed three iterations of the membrane affinity purification experiment, each with slight changes to the protocol to try and improve the enrichment or identification of membrane proteins. Samples from the first two experiments were quantified using label-free quantification (LFQ), identifying 58 and 135 proteins that were at least 2-fold enriched in the tubule samples relative to the control samples (Fig. **2a,b**, Supporting Information Tables **S1-S2**). Quantification using LFQ, however, can suffer from Poisson noise for lower-abundance proteins, leading some low-abundance proteins to appear enriched or depleted in a given sample due to differences in random run-to-run peptide sampling rather than differences in actual abundance in each sample (O'Connell *et al.*, 2018). We therefore set a minimum abundance threshold for proteins to be considered hits in those experiments, which reduced the number of 2-fold-enriched hits in the first two experiments to 22 and 92, respectively. We performed a third iteration of the membrane purification experiment using tandem mass tag (TMT) labeling to better quantify lower-

abundance proteins in our samples. This TMT experiment yielded 14 proteins that were at least 2-fold enriched in the tubule samples (Fig. **2c**, Supporting Information Table **S3**).

The highest-confidence hits from the membrane affinity purification experiments are listed in Table **1**. These highest-confidence hits were selected on the basis of being 2-fold enriched in the tubule samples in at least two of our three experiments. Four previously-known tubule proteins were among these proteins: the two bait proteins, RBMP1 and RBMP2, the carbonic anhydrase CAH3 (Sinetova *et al.*, 2012), and MITH1 (Hennacy *et al.*, 2024).

Less-highly-enriched were proteins such as HCF136 (Cre06.g273700) and TEF14 (Cre06.g256250), which are photosystem or photosystem-associated components that have been shown to be enriched in, but not exclusively localized to, the pyrenoid tubules (Mackinder, 2017; He *et al.*, 2023; Wang *et al.*, 2023), or CAS1 (Cre12.g497300), a calcium-sensing protein which is found throughout the chloroplast under high CO_2 but relocalizes to the tubules under the growth conditions used in our study (Wang *et al.*, 2016) (Supporting Information Tables **S1-S3**).

Importantly, our results are consistent with the enrichment of proteins based on membrane proximity rather than direct protein-protein interaction, as we were able to identify proteins not seen in traditional detergent-based affinity purification. Neither MITH1 nor CAH3 co-immunoprecipitated with RBMP1 or RBMP2 in a detergent-based affinity purification (Supporting Information Table **S4**), yet both are enriched in our tubule samples (Fig. **2**). The presence of CAH3, a pyrenoid tubule-enriched luminal protein with no predicted transmembrane domains (Sinetova *et al.*, 2012), also suggests that we are able to capture proteins within the membrane lumen. Furthermore, RBMP1 and RBMP2 did not co-precipitate in detergent-based affinity purification (Fig. **1h**, Supporting Information Table **S4**), whereas they did co-precipitate in our first and third membrane purifications (Table **3**). Taken together, these results indicate that our protocol is able to isolate and identify tubule membrane proteins that are not captured by traditional affinity purification approaches.

Identification of novel candidate tubule proteins

In addition to the previously-known tubule proteins, the top hits included two novel candidate tubule proteins: Low-CO_2-induced 16, also known as Early Light-Induced 4 (LCI16/ELI4; Cre02.g143550) and Cre10.g452250. LCI16 has a chlorophyll-binding domain which is

homologous to light-harvesting complex–like proteins present across plant and algal species (Rochaix & Bassi, 2019). These proteins are often induced by various abiotic stresses such as high light, high salinity, and high temperature; and function in photoprotection and assembly/repair of photosystems (Montané & Kloppstech, 2000; Rochaix & Bassi, 2019). Consistent with a potential function in tubules, LCI16 showed a similar pattern of diurnal mRNA expression to those of other tubule proteins, including RBMP1, RBMP2, and SAGA1, with a peak right after dawn (Supporting Information Fig. **S1**) (Strenkert *et al.*, 2019).

Cre10.g452250, which we named Pyrenoid Membrane-Enriched 1 (PME1), does not have any homologs we could identify. However, it does have a putative PRICHEXTENSN-like domain (Showalter *et al.*, 2010; Guo *et al.*, 2014) (Goodstein *et al.*, 2012; Craig *et al.*, 2023), a poorly-characterized proline-rich domain also found in RBMP1 and RBMP2. Additionally, although its expression levels were lower, PME1 also showed a peak in mRNA levels at or just before dawn, similar to LCI16, RBMP1, RBMP2, and SAGA1 (Supporting Information Fig. **S1**) (Strenkert *et al.*, 2019), further supporting a potential function in pyrenoid tubules.

Given the presence of LCI16 and PME1 in our tubule proteome and the similarities they share with other known tubule proteins, we decided to further characterize these novel tubule candidates to validate their tubule localization and determine if they impact pyrenoid tubule biogenesis.

Fluorescently-tagged LCI16 localizes to the pyrenoid-traversing membranes

To confirm that our novel tubule candidates are localized to the pyrenoid tubules, we created constructs to express each gene tagged with a Venus fluorophore and transformed each construct into wild-type cells (CC-4533). Cells transformed with PME1-Venus-3×FLAG constructs consistently showed antibiotic resistance but failed to express detectable levels of PME1-Venus-3×FLAG, possibly due to the lower expression levels of PME1 (Strenkert *et al.*, 2019). Thus, we focused our efforts on characterizing LCI16-Venus-3×FLAG transformants, which yielded detectable fluorescence.

We observed via fluorescence microscopy that LCI16-Venus-3×FLAG localizes to the center of the pyrenoid (Fig. **3a**). Its localization pattern was similar to those of RBMP1-Venus-3×FLAG and RBMP2-Venus-3×FLAG (Fig. **1d,e**) in being more compact and more heterogeneous than matrix-localized proteins such as Rubisco (Hennacy *et al.*, 2024). Based on this localization

pattern and LCI16's enrichment in our pyrenoid-traversing membrane proteome (Fig. **2** and Table **3**), we conclude that LCI16 localizes to pyrenoid-traversing membranes.

LCI16 physically interacts with RBMP2 and PME1

To further investigate the role of LCI16 in the tubule membranes, we performed a traditional detergent-based affinity purification using LCI16-Venus-3×FLAG as bait to determine what proteins it directly interacts with (Fig. **3b**, Supporting Information Table **S5**). In this experiment, the top two interactors of LCI16 were PME1 and RBMP2, indicating that these three proteins directly or indirectly physically interact in one or more protein complexes and providing additional support for PME1's tubule localization.

Our previous detergent-based RBMP1-Venus-3×FLAG and RBMP2-Venus-3×FLAG affinity purifications did not identify LCI16 or PME1 as highly enriched (Supporting Information Table **S4**). However, previously-published proteomic data from diurnally-grown cells suggest that RBMP2 may be more abundant than LCI16 or PME1 (Supporting Information Table **S1**) (Strenkert *et al.*, 2019). This raises the possibility that a large proportion of LCI16 and PME1 may be bound to RBMP2 even while the majority of RBMP2 is not bound to LCI16 or PME1. Unfortunately, due to our inability to produce a PME1-Venus-3×FLAG strain, we were unable to affinity purify PME1 to determine if all three proteins form a single complex or if LCI16 interacts with RBMP2 and PME1 separately.

Transmission electron microscopy (TEM) of insertional mutants in LCI16 and PME1

To assess the potential role(s) of LCI16 and PME1, we examined pyrenoid morphology in mutant strains lacking expression of each protein using transmission electron microscopy (TEM). We confirmed the insertion sites in one *lci16* and three *pme1* mutants by PCR (Supporting Information Fig. **S2**) and examined all mutants by electron microscopy. Unlike *mith1* and *saga1* mutants, which have the most-severe tubule-related defects observed in *C. reinhardtii* to date—with most Rubisco condensates entirely lacking tubules (Hennacy *et al.*, 2024)—the *lci16* and *pme1* mutants examined by TEM showed wild-type pyrenoid morphology. We regularly observed only one pyrenoid per cell, and we could observe central reticulated regions (Fig. **4b,e,h**) and peripheral cylindrical tubules with minitubules (Fig. **4c,f,i**, Supporting Information Figure **S3**) that were indistinguishable from those in wild-type cells. These results indicate that LCI16 and PME1 are not required for normal tubule morphology under our culture conditions, and suggest that they function in processes unrelated to tubule biogenesis.

Discussion

In this study, we enriched pyrenoid-traversing membrane fragments from *C. reinhardtii* and identified their associated proteins. From this dataset, we further characterized two novel tubule protein candidates, LCI16 and PME1.

Our membrane affinity purification approach overcame the challenge that pyrenoid tubules are contiguous with—and vastly less abundant than—the thylakoid membranes, impeding their isolation by traditional membrane fractionation methods (Bailyes *et al.*, 1997; Avila *et al.*, 2015). Our protocol overcame this challenge by enriching specific membrane subdomains based on the presence of a known resident protein, allowing us to identify novel protein components of the chosen membrane starting with only the identity of two of its protein components. The limitations of our implementation included low-number sampling noise due to analysis of the first two experiments by label-free mass spectrometry, which limited our ability to detect lower-abundance proteins; and changes to the protocol over the three iterations, which we think contributed to variability in hits between the three iterations. With further improvements, we believe our approach could be applied to determine the protein composition of other membrane domains on a sub-organellar level.

One of the proteins identified by our protocol is Low-CO_2-Induced 16 (LCI16), also known as Early Light-Induced 4 (ELI4). LCI16 has a LHC-like domain homologous to those found in the stress-related LHCs (LHCSR) and Early Light-Induced Protein (ELIP) families, which are characterized by a 3-helix chlorophyll-binding domain (Rochaix & Bassi, 2019; Levin & Schuster, 2023). These proteins are often induced by dark-to-light transitions, high light, and/or other abiotic stresses, and are typically involved in photoprotection via non-photochemical quenching (NPQ) as well as assembly of new photosystems or repair of damaged photosystems (Montané & Kloppstech, 2000; Rochaix & Bassi, 2019; Levin & Schuster, 2023). Given the localization of photosystem assembly factors to the periphery of the pyrenoid tubules (Mackinder, 2017) and its expression pattern (Strenkert *et al.*, 2019), LCI16 may assist in the synthesis of new photosystems in or near the pyrenoid. Future work will be needed to elucidate its precise role.

The other novel tubule protein we identified and characterized, PME1, interacts with LCI16 and possibly RBMP2. PME1 shares a predicted poorly-characterized PRICHEXTENSN domain with

RBMP1 and RBMP2. PRICHEXTENSN domains are found in plant extensins, a class of proteins associated with cell wall stability in plants. Plant extensins are typically characterized by PRICHEXTENSN domains made up of $SP_{3\text{-}4}$ repeats (Guo *et al.*, 2014), whereas in PME1 these repeats are even more highly-enriched in proline residues, containing $SP_{5\text{-}7}$ repeats interspersed with $(A/R/F)P_2$ repeats. Given the presence of this domain in multiple tubule proteins, it may play a role in tubule structure, function, or protein targeting to tubules. If the PRICHEXTENSN-like domains of PME1, RBMP1, and RBMP2 are partially redundant, generation of double or triple mutants among PME1, RBMP1, and RBMP2 may reveal phenotypes that would not be seen in the single mutants.

Interestingly, Alphafold3 (Abramson *et al.*, 2024) predicts that PME1's C-terminus contains a long amphipathic helix (Supporting Information Fig. **S4**). The structure prediction indicates this amphipathic helix may be involved in forming a homo-trimer, though this may be an artefact of Alphafold3's assumption that folding is taking place in an aqueous environment with no membranes. In addition to oligomerization (Truebestein & Leonard, 2016), amphipathic helices are also common among several families of membrane-binding and -shaping proteins, such as BAR domain proteins (Gallop *et al.*, 2006; Jao *et al.*, 2010) and reticulons (Brooks *et al.*, 2021), suggesting a potential mechanism for membrane binding in the C-terminal domain of PME1. Future work is needed to determine if this amphipathic helix is responsible for oligomerization or membrane binding.

Taken together, our results identify LCI16 and PME1 as novel pyrenoid-traversing membrane components, initiate their characterization, and suggest directions for future research into their functions. Our pyrenoid-traversing membrane proteome identifies known components and additional candidates, helping to prioritize proteins for future study. We hope these findings will ultimately contribute toward a mechanistic understanding of the pyrenoid, an organelle with a central role in the global carbon cycle.

Acknowledgments

We would like to thank Saw Kyin and Henry Shwe of the Princeton University Proteomics Core and the Thermo Fisher Scientific Center for Multiplexed Proteomics at Harvard Medical School (https://tcmp.hms.harvard.edu) for advice and help performing mass spectroscopy; John Schreiber and Paul Shao of the Princeton Imaging & Analysis Center for advice and technical support for electron microscopy; Michelle Warren-Williams for media preparation and propagating strains; Alice Lunardon, Cole Pacini, Weronika Patena, Victoria L. Crans, and Micah Burton for sharing reagents, experimental assistance, and feedback on the manuscript; Ned Wingreen, Fred Hughson, and members of the Jonikas laboratory for project feedback and helpful conversations; and Marie Bao, as part of Life Science Editors, for help with editing the manuscript. The authors acknowledge the use of the Imaging and Analysis Center (IAC) operated by the Princeton Materials Institute at Princeton University, which is supported in part by the Princeton Center for Complex Materials (PCCM), a National Science Foundation (NSF) Materials Research Science and Engineering Center (MRSEC; DMR-2011750). Research reported in this paper was supported by the Bill and Melinda Gates Foundation grant INV-054558, National Science Foundation grants MCB-1935444 and MCB-1914989, and NIGMS of the National Institutes of Health grants 1R01GM140032-01 and T32GM007388. The content is solely the responsibility of the authors and does not necessarily represent the official views of the National Institutes of Health. MCJ is a Howard Hughes Medical Institute Investigator.

Competing Interests

None declared.

Author contributions

EF and MCJ planned and conceived of and planned the project. EF, ERC, KD, and SLE performed the membrane purification experiments and EF analyzed the mass spectrometry data. EF performed the TEM imaging and growth assays. LW performed detergent-based affinity purifications; LW and AG performed fluorescence microscopy. AL, CP, and WP generated and mapped the *lci16* insertional mutants. EF and MCJ wrote the manuscript.

Data Availability

The data that supports the findings of this study are available in Supporting Information Tables S1-5 included with this article.

References

Abramson J, Adler J, Dunger J, Evans R, Green T, Pritzel A, Ronneberger O, Willmore L, Ballard AJ, Bambrick J, *et al.* 2024. Accurate structure prediction of biomolecular interactions with AlphaFold 3. *Nature* **630**: 493–500.

Avila JR, Lee JS, Torii KU. **2015**. Co-Immunoprecipitation of Membrane-Bound Receptors. *The Arabidopsis Book / American Society of Plant Biologists* **13**: e0180.

Bailyes EM, Navé BT, Soos MA, Orr SR, Hayward AC, Siddle K. **1997**. Insulin receptor/IGF-I receptor hybrids are widely distributed in mammalian tissues: quantification of individual receptor species by selective immunoprecipitation and immunoblotting. *Biochemical Journal* **327**: 209–215.

Barrett J, Girr P, Mackinder LCM. **2021**. Pyrenoids: CO2-fixing phase separated liquid organelles. *Biochimica et Biophysica Acta (BBA) - Molecular Cell Research* **1868**: 118949.

Beardall J, Raven JA. **2020**. Structural and Biochemical Features of Carbon Acquisition in Algae. In: Larkum AWD, Grossman AR, Raven JA, eds. Advances in Photosynthesis and Respiration – Including Bioenergy and Related Processes. Photosynthesis in Algae: Biochemical and Physiological Mechanisms. 141–160.

Behnke J-S, Urner LH. **2023**. Emergence of mass spectrometry detergents for membrane proteomics. *Analytical and Bioanalytical Chemistry* **415**: 3897–3909.

Brooks RL, Mistry CS, Dixon AM. **2021**. Curvature sensing amphipathic helix in the C-terminus of RTNLB13 is conserved in all endoplasmic reticulum shaping reticulons in Arabidopsis thaliana. *Scientific Reports* **11**: 6326.

Caspari OD, Meyer MT, Tolleter D, Wittkopp TM, Cunniffe NJ, Lawson T, Grossman AR, Griffiths H. **2017**. Pyrenoid loss in Chlamydomonas reinhardtii causes limitations in CO2 supply, but not thylakoid operating efficiency. *Journal of Experimental Botany* **68**: 3903–3913.

Craig RJ, Gallaher SD, Shu S, Salomé PA, Jenkins JW, Blaby-Haas CE, Purvine SO, O'Donnell S, Barry K, Grimwood J, *et al.* 2023. The Chlamydomonas Genome Project,

version 6: Reference assemblies for mating-type plus and minus strains reveal extensive structural mutation in the laboratory. *The Plant Cell* **35**: 644–672.

Ellis RJ. **1979**. The most abundant protein in the world. *Trends in Biochemical Sciences* **4**: 241–244.

Engel BD, Schaffer M, Cuellar LK, Villa E, Pitzko JM, Baumeister W. **2015**. Chlamydomonas chloroplast revealed by in situ cryo-electron tomography. *eLife* **4**.

Fei C, Wilson AT, Mangan NM, Wingreen NS, Jonikas MC. **2022**. Modelling the pyrenoid-based CO2-concentrating mechanism provides insights into its operating principles and a roadmap for its engineering into crops. *Nature Plants* **8**: 583–595.

Field CB, Behrenfeld MJ, Randerson JT, Falkowski P. **1998**. Primary Production of the Biosphere: Integrating Terrestrial and Oceanic Components. *Science* **281**: 237–240.

Flamholz AI, Prywes N, Moran U, Davidi D, Bar-On YM, Oltrogge LM, Alves R, Savage D, Milo R. **2019**. Revisiting Trade-offs between Rubisco Kinetic Parameters. *Biochemistry* **58**: 3365–3376.

Freeman Rosenzweig ES, Xu B, Cuellar LK, Martinez-Sanchez A, Schaffer M, Strauss M, Cartwright HN, Ronceray P, Plitzko JM, Förster F, *et al.* 2017. The Eukaryotic CO2-Concentrating Organelle Is Liquid-like and Exhibits Dynamic Reorganization. *Cell* **171**: 148-162.e19.

Gallop JL, Jao CC, Kent HM, Butler PJG, Evans PR, Langen R, McMahon HT. **2006**. Mechanism of endophilin N-BAR domain-mediated membrane curvature. *The EMBO journal* **25**: 2898–2910.

Goodenough UW. **1970**. Chloroplast Division and Pyrenoid Formation in Chlamydomonas Reinhardi. *Journal of Phycology* **6**: 1–6.

Goodenough UW, Levine RP. **1970**. CHLOROPLAST STRUCTURE AND FUNCTION IN ac-20, A MUTANT STRAIN OF CHLAMYDOMONAS REINHARDI□: III. Chloroplast Ribosomes and Membrane Organization. *Journal of Cell Biology* **44**: 547–562.

Goodstein DM, Shu S, Howson R, Neupane R, Hayes RD, Fazo J, Mitros T, Dirks W, Hellsten U, Putnam N, *et al.* 2012. Phytozome: a comparative platform for green plant genomics. *Nucleic Acids Research* **40**: D1178–D1186.

Guo L, Chen Y, Ye N, Dai X, Yang W, Yin T. **2014**. Differential retention and expansion of the ancestral genes associated with the paleopolyploidies in modern rosid plants, as revealed by analysis of the extensins super-gene family. *BMC Genomics* **15**: 612.

Hatch MD. **1987**. C4 photosynthesis: a unique blend of modified biochemistry, anatomy and ultrastructure. *Biochimica et Biophysica Acta (BBA) - Reviews on Bioenergetics* **895**: 81–106.

He S, Chou H-T, Matthies D, Wunder T, Meyer MT, Atkinson N, Martinez-Sanchez A, Jeffrey PD, Port SA, Patena W, *et al.* 2020. The structural basis of Rubisco phase separation in the pyrenoid. *Nature Plants* **6**: 1480–1490.

He S, Crans VL, Jonikas MC. **2023**. The pyrenoid: the eukaryotic CO2-concentrating organelle. *The Plant Cell* **35**: 3236–3259.

Hennacy JH, Atkinson N, Kayser-Browne A, Ergun SL, Franklin E, Wang L, Kafri M, Fauser F, Vilarrasa-Blasi J, Jinkerson RE, *et al.* 2024. Biogenesis, engineering and function of membranes in the CO2-fixing pyrenoid. : 2024.08.08.603944.

Jao CC, Hegde BG, Gallop JL, Hegde PB, McMahon HT, Haworth IS, Langen R. **2010**. Roles of amphipathic helices and the bin/amphiphysin/rvs (BAR) domain of endophilin in membrane curvature generation. *The Journal of Biological Chemistry* **285**: 20164–20170.

Karlsson J, Clarke AK, Chen ZY, Hugghins SY, Park YI, Husic HD, Moroney JV, Samuelsson G. **1998**. A novel alpha-type carbonic anhydrase associated with the thylakoid membrane in Chlamydomonas reinhardtii is required for growth at ambient CO2. *The EMBO Journal* **17**: 1208–1216.

Kyte J, Doolittle RF. **1982**. A simple method for displaying the hydropathic character of a protein. *Journal of Molecular Biology* **157**: 105–132.

Lau CS, Dowle A, Thomas GH, Girr P, Mackinder LCM. **2023**. A phase-separated CO2-fixing pyrenoid proteome determined by TurboID in Chlamydomonas reinhardtii. *The Plant Cell* **35**: 3260–3279.

Levin G, Schuster G. **2023**. LHC-like Proteins: The Guardians of Photosynthesis. *International Journal of Molecular Sciences* **24**: 2503.

Li X, Patena W, Fauser F, Jinkerson RE, Saroussi S, Meyer MT, Ivanova N, Robertson JM, Yue R, Zhang R, *et al.* 2019. A genome-wide algal mutant library and functional screen identifies genes required for eukaryotic photosynthesis. *Nature Genetics* **51**: 627–635.

Li J, Van Vranken JG, Pontano Vaites L, Schweppe DK, Huttlin EL, Etienne C, Nandhikonda P, Viner R, Robitaille AM, Thompson AH, *et al.* 2020. TMTpro reagents: a set of isobaric labeling mass tags enables simultaneous proteome-wide measurements across 16 samples. *Nature Methods* **17**: 399–404.

Lüttge U. **2004**. Ecophysiology of Crassulacean Acid Metabolism (CAM). *Annals of Botany* **93**: 629–652.

Ma Y, Pollock SV, Xiao Y, Cunnusamy K, Moroney JV. **2011**. Identification of a Novel Gene, CIA6, Required for Normal Pyrenoid Formation in Chlamydomonas reinhardtii. *Plant Physiology* **156**: 884–896.

Mackinder L. **2017**. A Spatial Interactome Reveals the Protein Organization of the Algal CO2 Concentrating Mechanism. Mackinder et al. *Cell* **171**: 133-147.e14.

Mackinder LCM, Meyer MT, Mettler-Altmann T, Chen VK, Mitchell MC, Caspari O, Rosenzweig ESF, Pallesen L, Reeves G, Itakura A, *et al.* 2016. A repeat protein links Rubisco to form the eukaryotic carbon-concentrating organelle. *Proceedings of the National Academy of Sciences* **113**: 5958–5963.

McAlister GC, Huttlin EL, Haas W, Ting L, Jedrychowski MP, Rogers JC, Kuhn K, Pike I, Grothe RA, Blethrow JD, *et al.* 2012. Increasing the Multiplexing Capacity of TMTs Using Reporter Ion Isotopologues with Isobaric Masses. *Analytical Chemistry* **84**: 7469–7478.

Meyer MT, Goudet MMM, Griffiths H. **2020a**. The Algal Pyrenoid. In: Larkum AWD, Grossman AR, Raven JA, eds. Advances in Photosynthesis and Respiration – Including Bioenergy and Related Processes. Photosynthesis in Algae: Biochemical and Physiological Mechanisms. 179–203.

Meyer MT, Itakura AK, Patena W, Wang L, He S, Emrich-Mills T, Lau CS, Yates G, Mackinder LCM, Jonikas MC. **2020b**. Assembly of the algal CO2-fixing organelle, the pyrenoid, is guided by a Rubisco-binding motif. *Science Advances* **6**: eabd2408.

Meyer K, Selbach M. **2015**. Quantitative affinity purification mass spectrometry: a versatile technology to study protein–protein interactions. *Frontiers in Genetics* **6**: 237.

Montané M-H, Kloppstech K. **2000**. The family of light-harvesting-related proteins (LHCs, ELIPs, HLIPs): was the harvesting of light their primary function? *Gene* **258**: 1–8.

Morris JH, Knudsen GM, Verschueren E, Johnson JR, Cimermancic P, Greninger AL, Pico AR. **2014**. Affinity purification–mass spectrometry and network analysis to understand protein-protein interactions. *Nature protocols* **9**: 2539–2554.

O'Connell JD, Paulo JA, O'Brien JJ, Gygi SP. **2018**. Proteome-Wide Evaluation of Two Common Protein Quantification Methods. *Journal of Proteome Research* **17**: 1934–1942.

Raven JA. **1997**. CO2-concentrating mechanisms: a direct role for thylakoid lumen acidification? *Plant, Cell & Environment* **20**: 147–154.

Raven JA, Beardall J, Sánchez-Baracaldo P. **2017**. The possible evolution and future of CO2-concentrating mechanisms. *Journal of Experimental Botany* **68**: 3701–3716.

Rawat M, Henk MC, Lavigne LL, Moroney JV. **1996**. Chlamydomonas reinhardtii mutants without ribulose-1,5-bisphosphate carboxylase-oxygenase lack a detectable pyrenoid. *Planta* **198**: 263–270.

Rochaix J-D, Bassi R. **2019**. LHC-like proteins involved in stress responses and biogenesis/repair of the photosynthetic apparatus. *Biochemical Journal* **476**: 581–593.

Sage RF, Sage TL, Kocacinar F. **2012**. Photorespiration and the evolution of C4 photosynthesis. *Annu. Rev. Plant Biol.* **63**: 19–47.

Schindelin J, Arganda-Carreras I, Frise E, Kaynig V, Longair M, Pietzsch T, Preibisch S, Rueden C, Saalfeld S, Schmid B, *et al.* 2012. Fiji: an open-source platform for biological-image analysis. *Nature Methods* **9**: 676–682.

Showalter AM, Keppler B, Lichtenberg J, Gu D, Welch LR. **2010**. A Bioinformatics Approach to the Identification, Classification, and Analysis of Hydroxyproline-Rich Glycoproteins. *Plant Physiology* **153**: 485–513.

Sinetova MA, Kupriyanova EV, Markelova AG, Allakhverdiev SI, Pronina NA. **2012**. Identification and functional role of the carbonic anhydrase Cah3 in thylakoid membranes of pyrenoid of Chlamydomonas reinhardtii. *Biochimica et biophysica acta* **1817**: 1248.

Strenkert D, Schmollinger S, Gallaher SD, Salomé PA, Purvine SO, Nicora CD, Mettler-Altmann T, Soubeyrand E, Weber APM, Lipton MS, *et al.* 2019. Multiomics resolution of molecular events during a day in the life of Chlamydomonas. *Proceedings of the National Academy of Sciences* **116**: 2374–2383.

Ting L, Rad R, Gygi SP, Haas W. **2011**. MS3 eliminates ratio distortion in isobaric multiplexed quantitative proteomics. *Nature Methods* **8**: 937–940.

Toyokawa C, Yamano T, Fukuzawa H. **2020**. Pyrenoid Starch Sheath Is Required for LCIB Localization and the CO_2 -Concentrating Mechanism in Green Algae. *Plant Physiology* **182**: 1883–1893.

Truebestein L, Leonard TA. **2016**. Coiled-coils: The long and short of it. *Bioessays* **38**: 903–916.

Wang L, Patena W, Van Baalen KA, Xie Y, Singer ER, Gavrilenko S, Warren-Williams M, Han L, Harrigan HR, Hartz LD, *et al.* 2023. A chloroplast protein atlas reveals punctate structures and spatial organization of biosynthetic pathways. *Cell* **186**: 3499-3518.e14.

Wang Y, Stessman DJ, Spalding MH. **2015**. The CO2 concentrating mechanism and photosynthetic carbon assimilation in limiting CO2: how Chlamydomonas works against the gradient. *The Plant Journal* **82**: 429–448.

Wang L, Yamano T, Takane S, Niikawa Y, Toyokawa C, Ozawa S, Tokutsu R, Takahashi Y, Minagawa J, Kanesaki Y, *et al.* 2016. Chloroplast-mediated regulation of CO2-concentrating mechanism by Ca2+-binding protein CAS in the green alga Chlamydomonas reinhardtii. *Proceedings of the National Academy of Sciences* **113**: 12586–12591.

Zhan Y, Marchand CH, Maes A, Mauries A, Sun Y, Dhaliwal JS, Uniacke J, Arragain S, Jiang H, Gold ND, *et al.* 2018. Pyrenoid functions revealed by proteomics in Chlamydomonas reinhardtii. *PLOS ONE* **13**: e0185039.

Zhang R, Patena W, Armbruster U, Gang SS, Blum SR, Jonikas MC. **2014**. High-Throughput Genotyping of Green Algal Mutants Reveals Random Distribution of Mutagenic Insertion Sites and Endonucleolytic Cleavage of Transforming DNA. *The Plant Cell* **26**: 1398–1409.

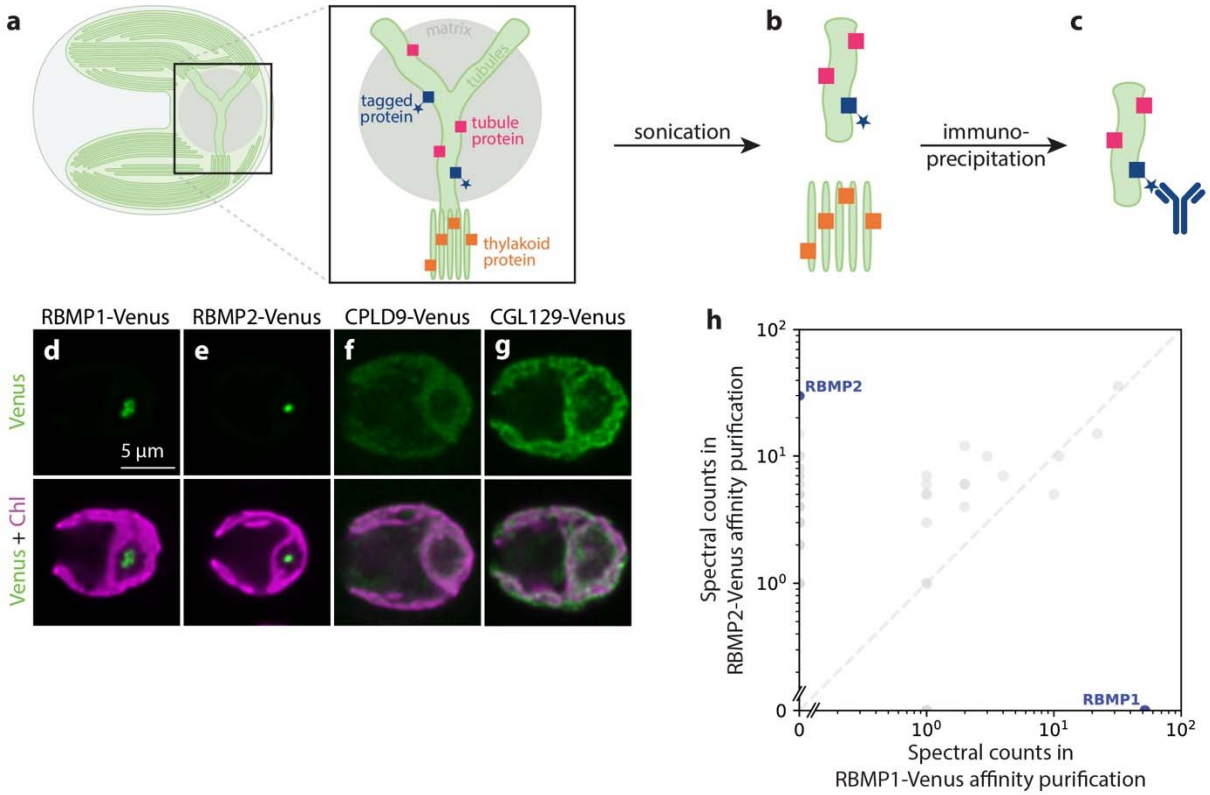

Figure 1: We adapted an affinity precipitation protocol to purify intact membranes. **a–c.** Schematic of the membrane affinity purification. **a.** Cartoon representation of a *C. reinhardtii* cell, with the pyrenoid in the base of the cup-shaped chloroplast. Inset: The pyrenoid is traversed by tubule membranes which are contiguous with but structurally distinct from the photosynthetic thylakoids. Colored squares represent the proteins localized to the membranes: blue squares with a star represent known tubule proteins tagged with a FLAG tag, pink squares represent all other proteins localized to the tubules and potentially pulled down by our experiment, and orange squares represent proteins mainly localized in the thylakoid membranes. **b.** By disrupting cellular membranes using sonication, we sought to create small membrane fragments whose protein composition was maintained. **c.** Membrane fragments containing tagged proteins were immunoprecipitated using an anti-FLAG antibody and their protein composition was determined by mass spectrometry. **d–g.** Confocal fluorescence images showing the localization of the FLAG-tagged proteins used as baits for the membrane affinity purification. Chlorophyll, a proxy for the presence of thylakoid membranes, is shown in magenta. The pyrenoid is in the low-chlorophyll region in the base of each cell. Venus signal is shown in green, representing the localization of the tubule **(d–e)** or thylakoid **(f–g)** bait proteins. **h.** Results of a detergent-based affinity purification show that the tubule bait proteins RBMP1-Venus and RBMP2-Venus do not co-precipitate using traditional affinity purification methods.

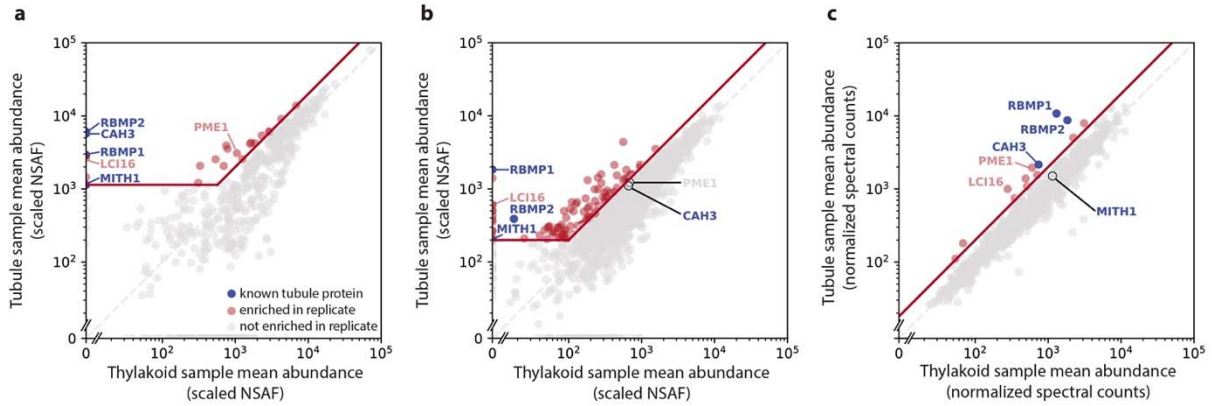

Figure 2: The membrane affinity purification experiment identified both known and novel tubule proteins.

Protein abundances in tubule samples vs. thylakoid samples for the three membrane affinity purification experiments. Blue points represent the known tubule proteins RBMP1, RBMP2, CAH3, and MITH1. The grey dashed lines represent y=x, at which proteins are equally abundant in both the tubule and thylakoid samples. The diagonal red line represents 2-fold enrichment in the tubule samples. The first two experiments **(a–b)** were quantified using label-free quantification, leading to significant noise among lower-abundance proteins. For these experiments, hits (red points) were defined as exceeding 2-fold enrichment in the tubule sample and exceeding a lower abundance threshold (horizontal red line). Proteins in the third membrane affinity purification **(c)** were quantified using tandem mass tagging, leading to better quantification of low abundance proteins. Thus, only 2-fold enrichment was required to be considered a hit. Proteins that are enriched in at least 2 experiments can be found in Table **3**.

Table 2: Proteins enriched in at least two membrane affinity purification experiments

		Experiment 1					Experiment 2					Experiment 3					
Locus	Gene Name	RBMP1	RBMP2	CPLD9	CGL129	fold enriched	RBMP1	RBMP2	CPLD9	CGL129	fold enriched	RBMP1	RBMP2	CPLD9	CGL129	fold enriched	enriched
Cre06.g261750	**RBMP1**	5548	281	0	0	INF	3678	0	0	0	INF	19792	1762	1159	1446	8.3	3
Cre09.g416850	**RBMP2**	3669	8470	0	0	INF	50	727	0	36	21.9	3429	13989	1818	1860	4.7	3
Cre02.g143550	LCI16	3312	2012	0	0	INF	908	312	0	0	INF	2066	710	478	504	2.8	3
Cre09.g415700	**CAH3**	5985	5454	0	0	INF	1642	565	549	772	1.7	2955	1346	702	777	2.9	2
Cre06.g259100	**MITH1**	704	1569	0	0	INF	0	399	0	0	INF	1640	1370	1173	1118	1.3	2
Cre10.g452250	PME1	1454	4711	1196	906	2.9	798	1646	801	563	1.8	1677	2240	651	555	3.2	2

Table 3. Proteins enriched in at least two membrane affinity purification experiments

Spectral counts in each affinity purification sample for the proteins identified as enriched in at least two out of the three membrane affinity purification experiments. These values are scaled normalized spectral abundance factor values for experiments 1 and 2, which were quantified using label-free quantification; and normalized spectral counts for experiment 3, which was quantified using tandem-mass-tagging. The names of previously-known tubule proteins are bolded.

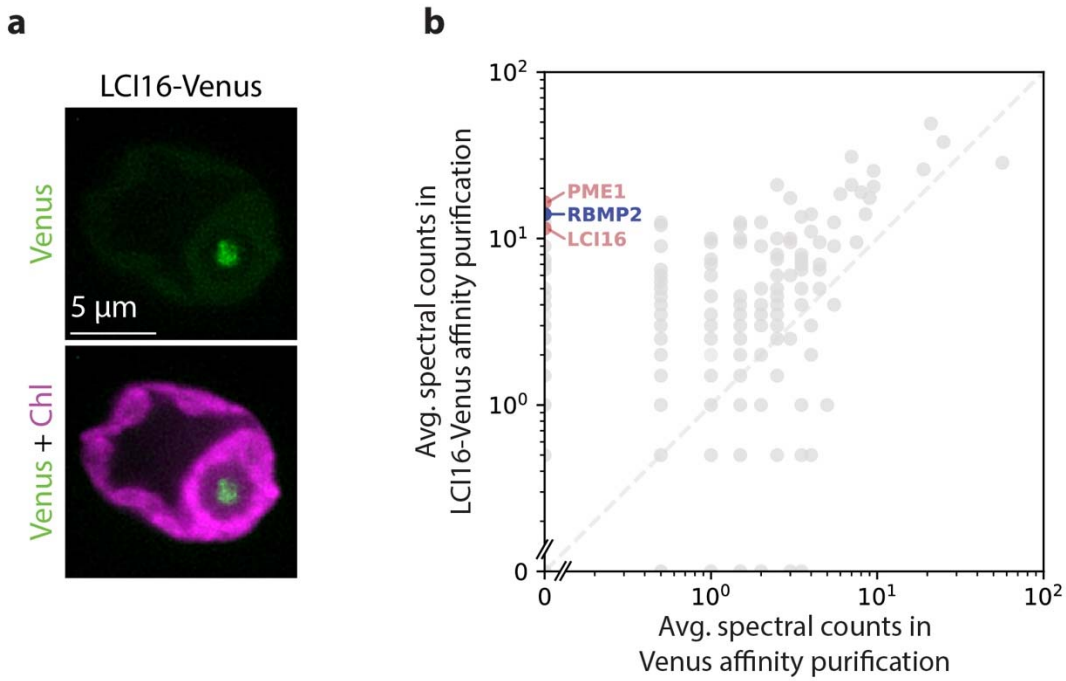

Figure 3: LCI16-Venus localizes to the pyrenoid tubules and co-precipitates RBMP2 and PME1.

a. Confocal images showing the localization of LCI16-Venus in the pyrenoid tubules. Green represents LCI16-Venus signal and magenta represents chlorophyll. **b**. Average spectral counts for a detergent-based affinity purification of LCI16-Venus compared to a control affinity purification of Venus alone. The blue point represents the known tubule protein RBMP2, while the red points represent the novel tubule components LCI16 and PME1.

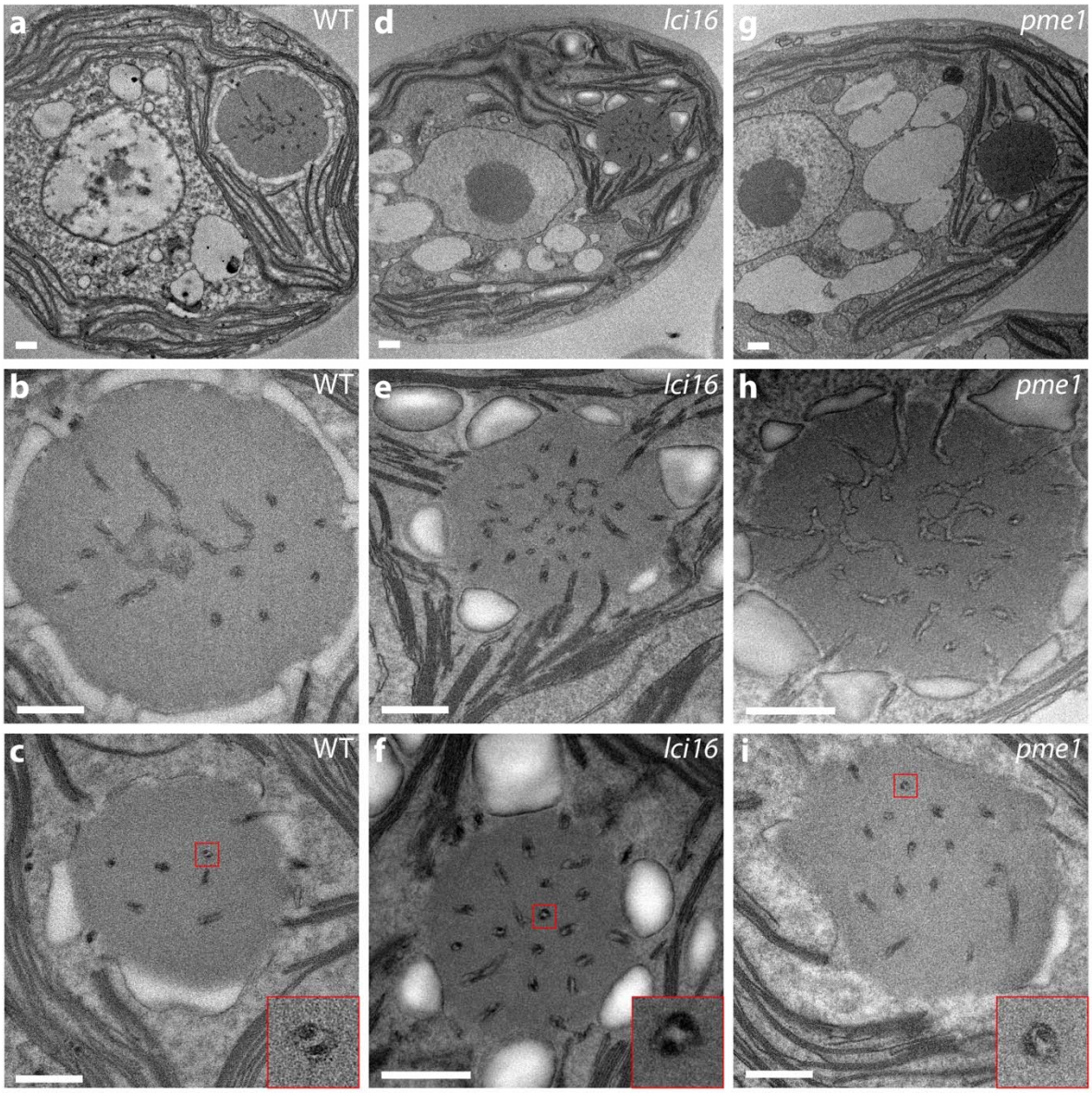

Figure 4: Transmission electron microscopy reveals normal pyrenoid morphology in insertional mutants of *lci16* and *pme1*.

Electron micrographs of wild type **(a–c)**, *lci16* **(d–f)**, and *pme1* **(g–i)** cells. Images of central slices of whole cells **(a,d,g)** show the single pyrenoid in its stereotyped location at the base of the cup-shaped chloroplast. Higher-magnification images of the pyrenoids **(b–c,e–f, h–i)** show tubules in all of the pyrenoids, including both the central reticulated region, characterized by three-way membrane junctions **(b,e,h)** and the peripheral minitubule-containing tubules **(c,f,i)**. 4x insets in **(c,f,i)** show individual tubules with visible minitubules. Pyrenoids in **(b,e,h)** represent the same cells as shown in **(a,d,g)**. Scale bars 500 nm.

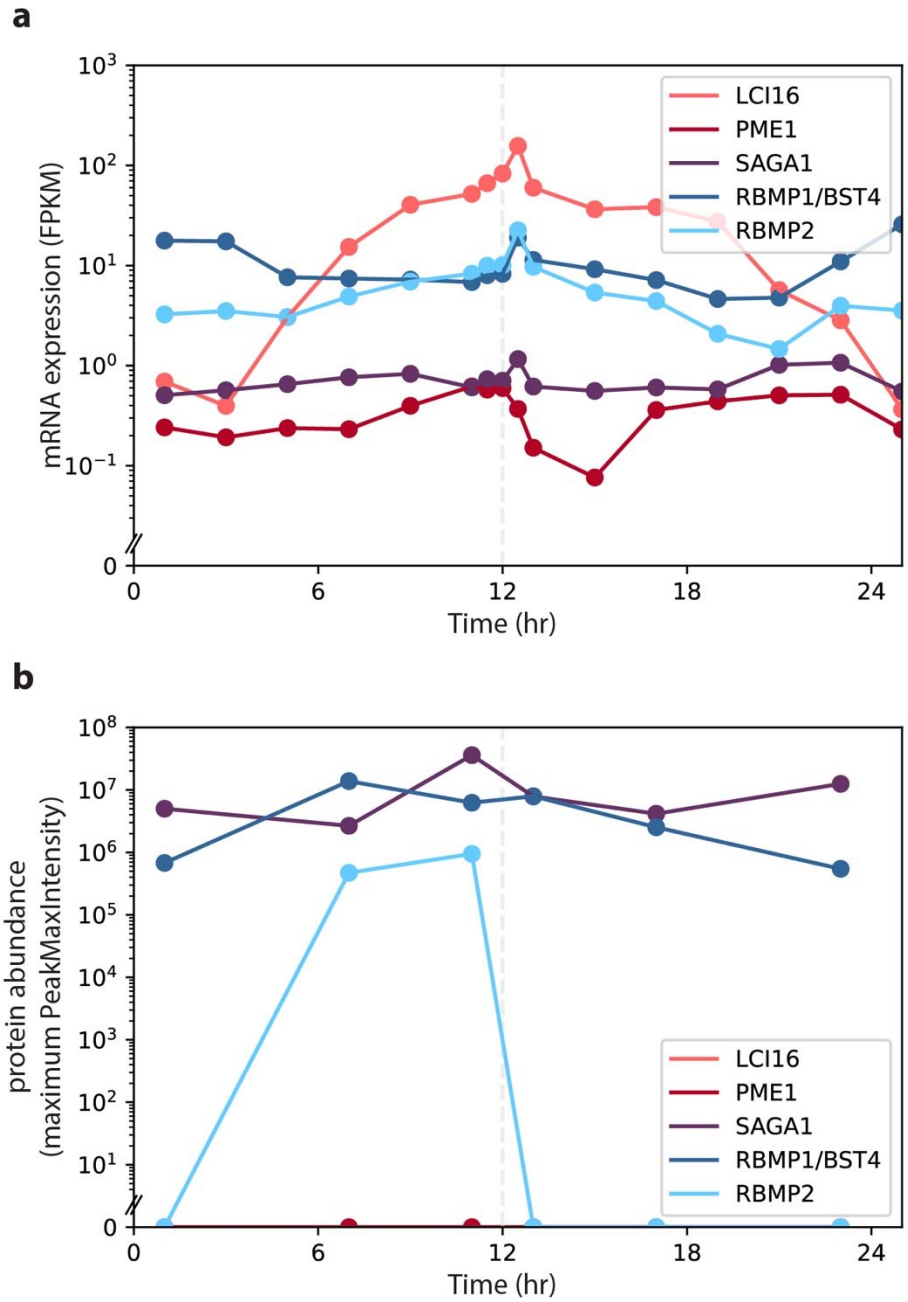

Supporting Information Figure S1: Transcript and protein levels

Transcriptomic and proteomic data from diurnally-grown *C. reinhardtii* cells measuring the abundance of mRNA (**a**) and protein (**b**) levels of the known pyrenoid tubule proteins RBMP1, RBMP2, and SAGA1 (blue/purple lines) compared to the novel tubule components LCI16 and PME1 (red/pink lines). Cells were synchronized and grown in a 12-hour light/12-hour dark cycle, with hour 12 corresponding to the onset of light. Based on data reported in (Strenkert *et al.*, 2019). **a.** mRNA levels of known and novel tubule proteins throughout the diurnal cell cycle.

Baseline mRNA levels differ for each gene, but each expression pattern shows a peak at (PME1) or directly after (RBMP1, RBMP2, SAGA1, LCI16) the onset of light. **b.** Protein abundance of known and novel tubule proteins throughout the diurnal cell cycle. The novel tubule proteins LCI16 and PME1 are not detected at any time point, while the known tubule proteins RBMP1, RBMP2, and SAGA1 are all detected at low levels, either consistently throughout the cell cycle (RBMP1 and SAGA1) or only in the dark (RBMP2)

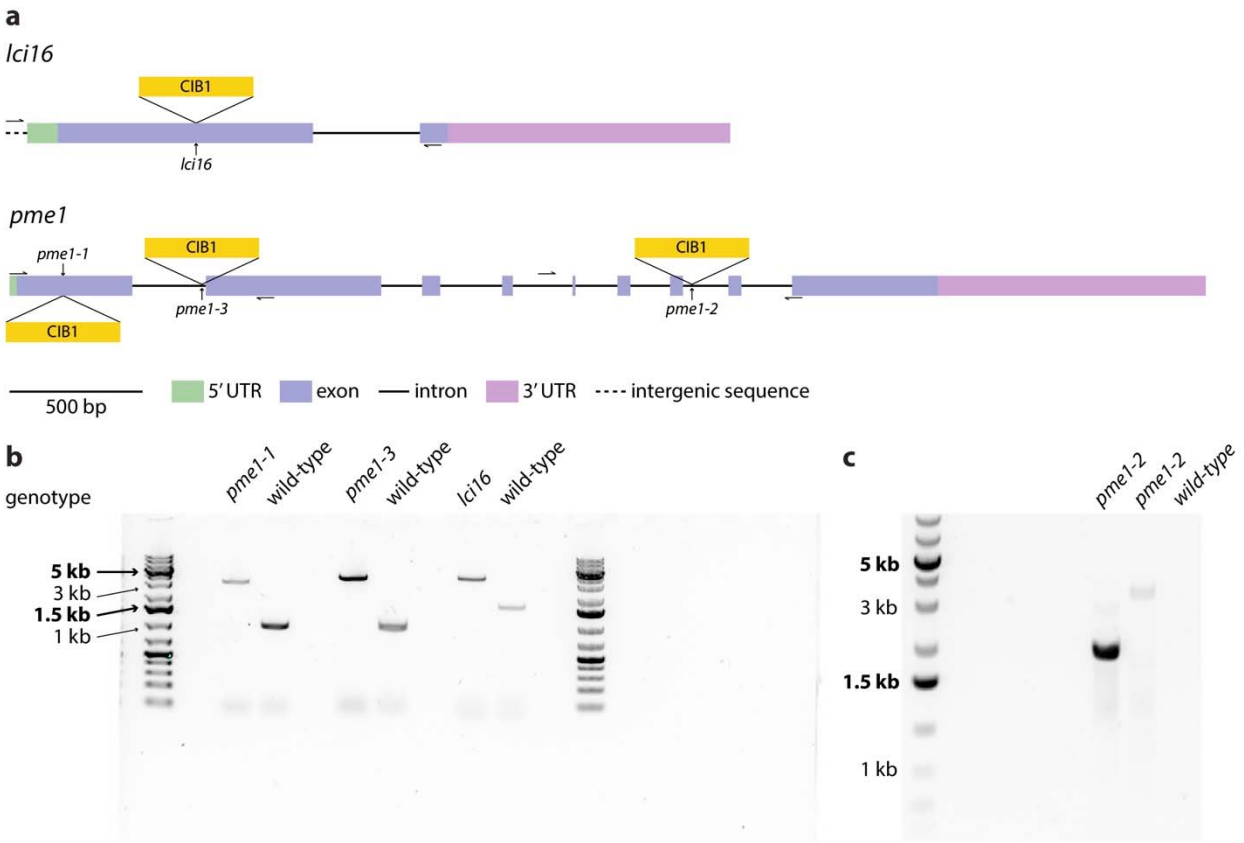

Supporting Information Figure S2: PCR verification of *lci16* and *pme1* insertional mutants

PCR verification of the insertions the *lci16* and *pme1* mutants. (**a**) Maps of the *LCI16* and *PME1* genomic loci showing the locations of the CIB1 insertion cassette and the primers used for PCR verification. The CIB1 cassette and primer sequences are not drawn to scale. (**b-c**) Agarose gels showing amplification across the insertion junction in genomic DNA purified from *pme1-1*, *pme1-3*, and *lci16* (**b**); and *pme1-2* (**c**). Expected amplicon lengths for wild-type gDNA were 1025 bp for *pme1-1* and *pme1-3* using the primers TIP.Z4.For/Rev; 1643 bp for *lci16* using the primers TS.Q.For/Rev; and 1014 bp for *pme1-2* using the primers TIP.Z2/3.For/Rev. For each strain in panel (**b**), the left lane shows the amplicon from the mutant's gDNA and the right lane shows the amplicon from wild-type gDNA using the same primers. Amplicon lengths for each mutant were in excess of 3,000 bp and were longer than the amplicons produced by the same primers in wild-type gDNA, confirming the presence of the insertion in each mutant. In panel (**c**), leftmost lane shows pme1-2 gDNA and a control set of primers, TS.Hb.For/Rev, which amplify a neutral locus at which there is no insertion; and the middle and right lanes show the *pme1-2* insertion junction amplified in *pme1-2* and wild-type gDNA, respectively. There was insufficient wild-type gDNA template to amplify the expected band in the rightmost lane, but the amplicon

721 from the *pme1-2* gDNA was well in excess of the expected length, confirming the presence of
722 the insertion. Primer sequences can be found in the Materials and Methods section.

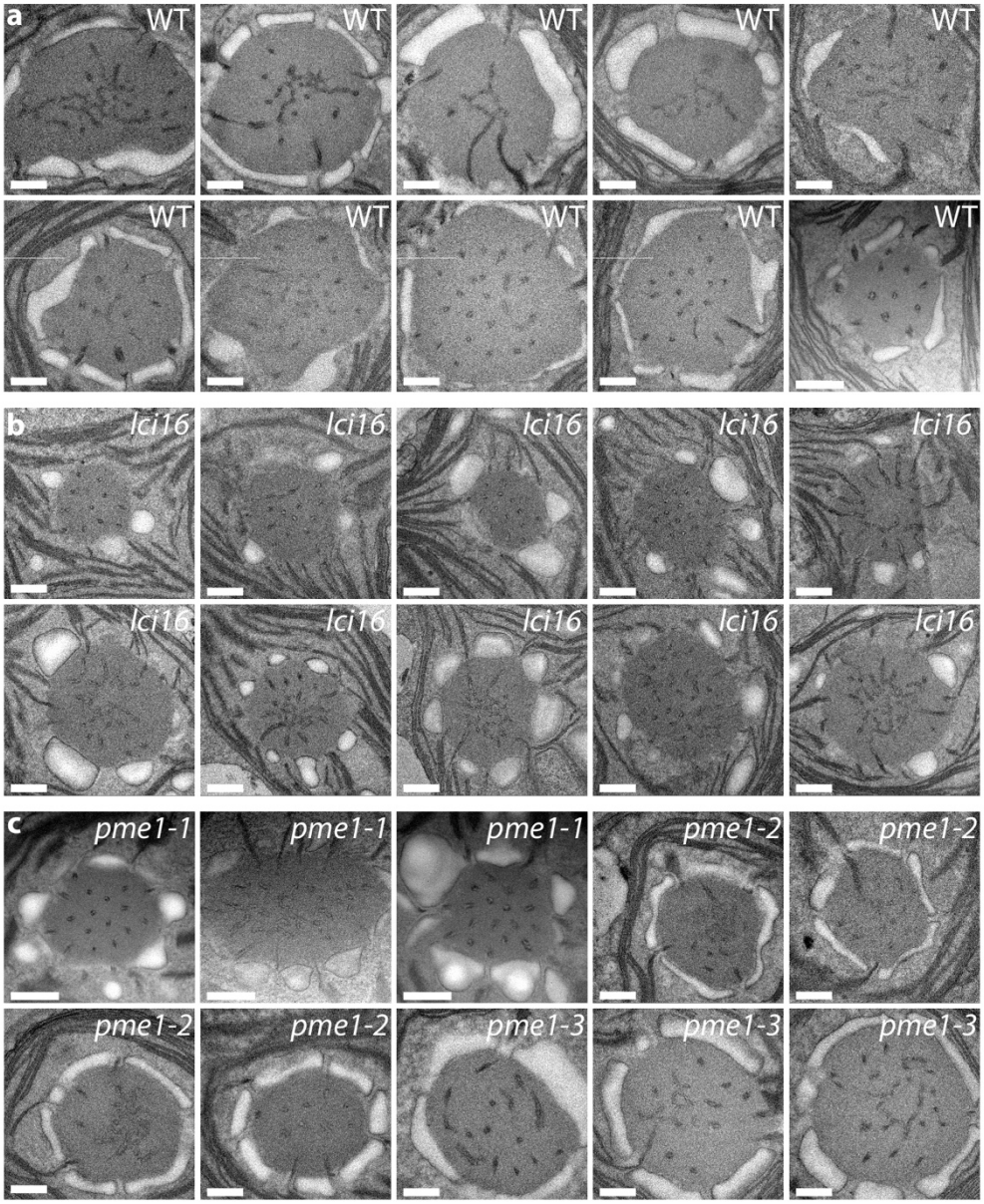

Supporting Information Figure S3: Additional TEM pyrenoid images of insertional mutants of *lci16* and *pme1*

Additional micrographs of wild-type (**a**), *lci16* (**b**), and *pme1* (**c**) pyrenoids, showing that lci16 and pme1 mutant pyrenoids contain central reticulated regions and minitubule-containing peripheral tubules indistinguishable from wild-type cells. Scale bars 500 nm.

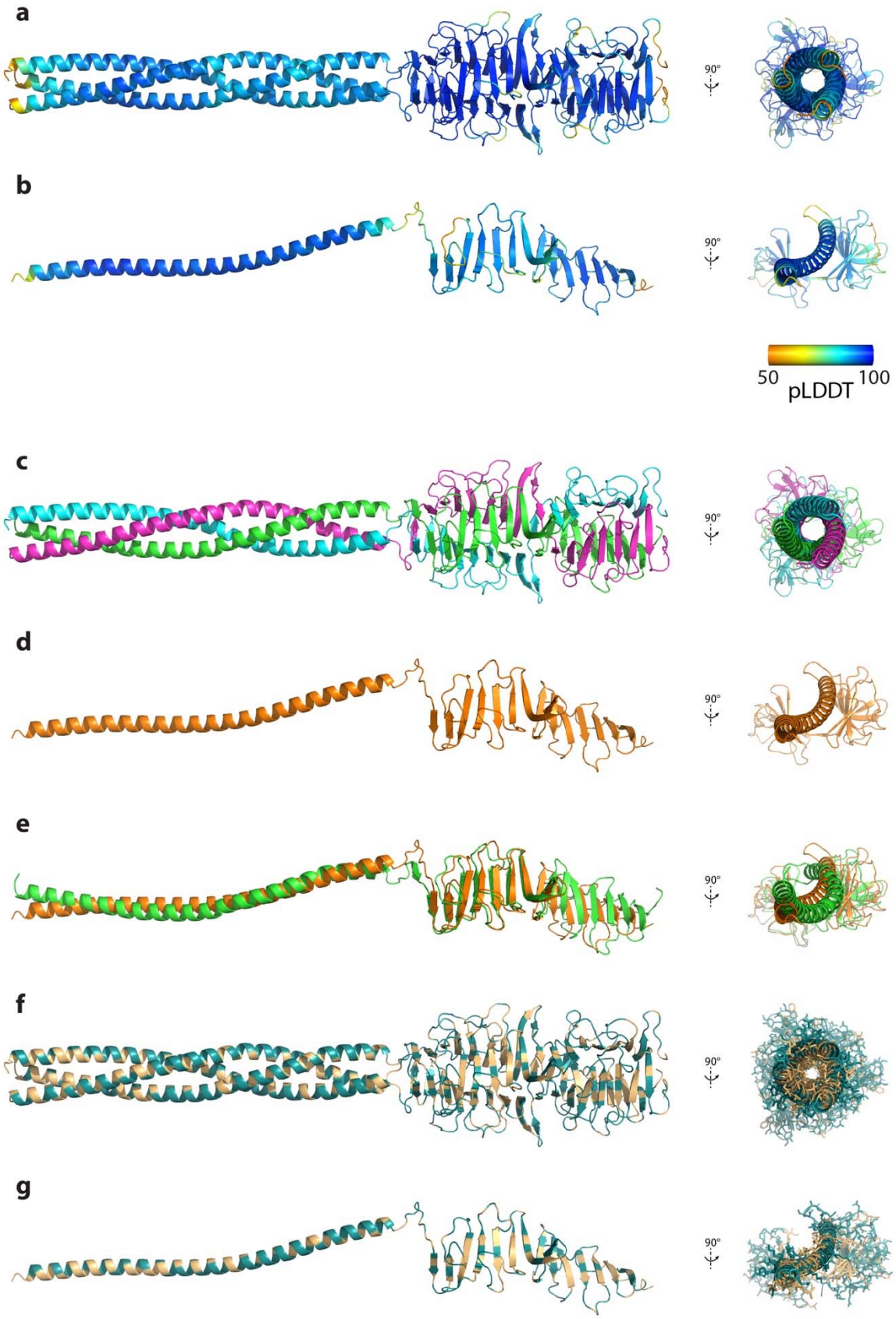

729

Supporting Information Figure S4: Alphafold3 predicts an amphipathic helix and beta sheet in PME1.

Alphafold3 predictions of a trimer **(a,c,f)** and monomer **(b,d,g)** of the residues 380–639 of PME1, the 260 residues at the C-terminus of PME1. **a–b**. The trimer **(a)** and monomer **(b)** colored according to the per-atom confidence metric pLDDT. Confidence scores for the entire structure are higher for the trimer (pTM = 0.83, iPTM = 0.82) than the monomer (pTM = 0.49). **c–e.** Cartoon representation of the extended helix and beta sheet of the predicted trimer **(c)**, in which the helices form a coiled coil and the beta sheets form a beta-barrel-like structure, and the monomer **(d)**, which takes on a similar conformation even in the absence of oligomerization, as shown by an alignment of the monomer with one subunit of the trimer **(e)**. **f–g.** The predicted trimer **(f)** and monomer **(g)** colored by Kyte-Doolittle hydrophobicity (Kyte & Doolittle, 1982), with hydrophilic residues colored deep teal and hydrophobic residues colored beige. In the 90-degree rotations showing the structure along the axis of the helix, side chain visualization has been added to show that the interior of the coiled coil contains almost exclusively hydrophobic residues while the exterior is almost entirely hydrophilic.